LAWRENCE
LIVERMORE
NATIONAL
LABORATORY

LLNL-JRNL-644944

Heterogeneous flow and brittle failure in shock-compressed silicon

R. F. Smith, C. A. Bolme, D. J. Erskine, P. M. Celliers, S. Ali, J. H. Eggert, S. L. Brygoo, B. D. Hammel, J. Wang, G. W. Collins

October 16, 2013

Journal of Applied Physics

Disclaimer

Heterogeneous flow and brittle failure in shock-compressed Silicon

R.F. Smith[1], C.A. Bolme[2], D.J. Erskine[1], P.M. Celliers[1], S. Ali[1, 3], J.H. Eggert[1], S.L. Brygoo[4], B.D. Hammel[1], J. Wang[5], G.W. Collins[1]

[1]*Lawrence Livermore National Laboratory, P.O. Box 808, Livermore, California 94551, USA*

[2]*Los Alamos National Laboratory, Los Alamos, New Mexico 87545, USA*

[3]*Department of Earth and Planetary Science, University of California, Berkeley, CA 94720, USA.*

[4]*CEA, DAM, DIF, F-91297 Arpajon, France.*

[5]*Department of Geosciences, Princeton University, Princeton, NJ 08544, USA.*

We combine a recently developed high-resolution two-dimensional (2D) imaging velocimetry technique (VISAR) with 1D VISAR measurements to construct a moving picture of heterogeneous deformation in shock-compressed single crystal silicon. The 2D VISAR takes an intensity snapshot of target velocity and reflectivity over a mm field-of-view while the compression history is simultaneously recorded by the 1D VISAR. Our data shows particle velocity surface roughening due to the anisotropic onset of plasticity and, above ~13 GPa, a structural phase transformation. Shock arrival at the Si free-surface is characterized by the formation of fracture networks and incipient velocity jetting.

I. Introduction

Understanding the nature and dynamics of heterogeneous flow in materials subjected to shock loading is important for many fields of research ranging from high-speed collisions to inertial confinement fusion studies. As reported here, the particle velocity field of a shock front propagating through a material may be altered significantly from mechanisms such as anisotropic sound speeds, phase transformations, plastic flow and brittle failure. The ability to quantify these effects has been limited by a lack of diagnostics able to provide simultaneous µm and ns spatial and temporal resolution velocity measurements on samples travelling at km/s speeds or greater. Since the early 1970's, the standard diagnostic in high-pressure dynamic compression experiments has been the velocity interferometer system of any reflector (VISAR) which measures shock, particle and sound velocities as a function of time.[1 2 3 4] This information allows researchers to constrain the equation-of-state[5] and quantify the deformation response associated with elastic-plastic[6 7] and structural phase transformations[8 9]. However, as VISAR systems are typically operated with a spatial resolution of zero (point VISAR),[5 6 8] or ~30-50 µm along a line (1D VISAR)[4] the effects of heterogeneous flow are not captured. Recently a new two-dimensional imaging velocimetry technique (2D VISAR) has been developed to measure the velocity roughness of shock fronts with ~10 m/s resolution and a spatial resolution of ~2.5 µm over a 0.8 mm field-of-view.[10 22] The 2D VISAR gives a ps "snapshot" of the velocity and target reflectivity field at a time after the arrival of a shock front at a reflecting interface. In this paper we combine the 1D and 2D VISAR systems to study heterogeneous flow and the formation of fracture networks in single crystal silicon. The 1D VISAR records the compression history of the sample while the 2D VISAR captures ps snapshots of the spatially resolved velocity and reflectivity maps.

Silicon is an ideal material to study the dynamics of heterogeneous flow due to the availability of high-purity, low dislocation density (< 10^5 cm^{-2}) and well-orientated single crystals.[11 12 13 14] Quasi-hydrostatic compression studies on silicon, which under ambient conditions has a diamond crystal structure, have revealed several pressure induced polymorphic phase transformations between ~13-18 GPa.[15] Under uniaxial shock compression Si exhibits high orientation-dependent elastic stresses with the onset of plastic deformation characterized by a near complete loss of shear strength and an orientation-independent deformation response.[7 16 17] However significant inconsistencies exist in the reported high-pressure response

of Si. In shock experiments, where wave speed measurements are used to determine the volume collapse associated with the phase transformation, very different compressibilities have been reported depending on whether the sample has a free-surface ($V/V_0 \sim 0.85$ at 16 GPa)[17] [18] or an impedance matched LiF VISAR window ($V/V_0 \sim 0.67$ at 16GPa).[16] In the work reported here we measure and compare the heterogeneous deformation response of shock loaded Si free-surface and Si/LiF samples. For Si/LiF samples our data show particle velocity surface roughening initially from the anisotropic onset of plasticity and again, above ~13 GPa, due to a structural phase transformation. For Si free-surface samples the onset of inelastic deformation is characterized by the formation of fracture networks and incipient velocity jetting.

The paper has the following layout. Section II describes the experimental method. Section III reports on three separate measurements: (a) Particle velocity measurements of spherical shock breakout from a 1 mm thick Si/LiF sample (b) Particle velocity measurements of planar shock breakout from a 0.3 mm thick Si/LiF sample (c) Free-surface velocity measurements of planar shock breakout from a 0.3 mm thick Si sample. A discussion of the data is presented in Section IV. Conclusions are reported in Section V.

II. Experimental method

a. Target design

The experiments described here were conducted on the Janus laser facility at the Lawrence Livermore National Laboratory in California. We report on two compression geometries to study the heterogeneous flow in single crystal Si [111]: a spherical shock and a spatially planar shock. The target design for the spherical shock experiments consists of 1 mm thick single crystal Si [111] and a 0.5 mm thick LiF [100] VISAR window with an estimated Si-LiF glue layer thickness of ~3 μm (Fig. 1(a)). A 527 nm laser beam with 300 J in 4 ns was focused down to overfill a 500 μm circular aperture and directly ablate the Si sample with an average intensity of $\sim 2.5 \times 10^{13}$ W/cm^2.[19] This geometry launches an initially circular pressure drive into the Si. Similar experiments were also conducted using Si [110] and [100] single crystals.

The target design for the planar shock experiments, as shown in Fig. 1(b), consists of 10 μm CH/50 μm Al/300 μm Si [111] and a 500 μm LiF window. A 6 ns square laser pulse with 250 J of energy directly ablates the 10 μm CH layer backed by 50 μm of Al. A kinoform phase plate

inserted into the Janus beam-line, produces a ~1 mm square, planar (ΔI/I ~ 5%) region at the focal plane. This setup ensures that a steady shock with ~4 ns duration, planar over a 1 mm square area, is launched into the Si sample.[20] The planar drive experiments were conducted with and without the LiF VISAR window. The good impedance match between Si and LiF substantially reduces the effect of wave interactions compared to free-surface Si samples. Due to the planar inertially confined nature of the ramp drive, our samples are in a state of uniaxial strain.

b. 1D VISAR

For all experiments, the spatial- and time-dependence of the transmitted compression wave velocity was recorded at the Si/LiF interface, $u_p(x,y,t)$, or the Si/vacuum free-surface, $u_{fs}(x,y,t)$, with the combined 1D and 2D VISAR setup as shown in Fig. 2. The 1D VISAR measures the sample interface velocity versus time along a 1 mm line at the target plane with a spatial resolution of ~30-50 μm and a spatial integration due to the line width of ~15 μm. The 1D VISAR employs a 50 ns 532 nm multimode probe beam, which is focused onto the target with an f/3 lens.[4] The frequency of the reflected light from the moving (shock-compressed) sample is Doppler shifted and the resultant phase change is detected through fringe shifts within the VISAR interferometer and recorded in time with an optical streak camera. The velocity sensitivity of the interference fringes recorded by the VISAR is controlled by inserting different lengths of fused silica etalons in one leg of the interferometer to alter the optical delay in that leg. In our experiments we used etalon lengths of 50.074 and 100.0169 mm to produce vacuum velocity-per-fringe (VPF) constants of 1.105 and 0.829 km/s. Two VISAR channels (only one shown in Fig. 2) with different velocity sensitivities were used to provide redundant data and resolve any ambiguities associated with sharp velocity jumps that exceed the time response of the system. For some experiments we increased the field-of-view to 2mm by employing an f/6 imaging system. Compression wave roughness can cause the local angle of the reflecting sample to eject the VISAR probe light outside of the collection angle of the imaging lens (no signal on data record). The multimode illumination design of the 1D VISAR ensures that a range of angles illuminates each spatial point of the target thereby making it less sensitive to loss of signal due to target roughness.[4]

c. 2D VISAR

The 2D VISAR employs the ~1 mJ, 3 ps, 400 nm frequency-doubled single mode output from a commercial Ti-sapphire laser system which, before illumination of the target, is injected into an input interferometer with a ~50 mm thick fused silica etalon (delay element) as shown in Fig. 2. This produces two 3 ps pulses with a temporal separation of 263 ps which are then focused onto the target. The 400 nm single mode 2D VISAR probe beam is combined with the 532 nm, 50 ns 1D VISAR probe beam via a dual band dichroic beamsplitter and imaged onto the sample with a common achromatic lens system. After reflection off the Si free-surface or Si/LiF interface the two 400 nm probe pulses are propagated through an output interferometer with a matched delay element. The output of this second interferometer contains a train of four 3 ps pulses with the central two pulses temporally and spatially overlapped to generate an interference pattern. The fringes produced are at most 50% visibility, but otherwise have the same fringe shift per target motion behavior of a traditional VISAR.[10 22]

Using the two outputs from the output interferometer and by controlling and selecting the polarization of the light we record four separate 2D images of the target plane on a 4000 × 4000 pixel cooled CCD chip with a 36×36 mm^2 active area and a 9 μm pixel size: s-polarized, s-polarized with 180° phase shift, p-polarized, p-polarized with 270° phase shift (see Fig. 3(a)).[21] The raw data in Fig. 3(a) records the emergence of a compression wave at the Si/LiF interface for the target described in Fig. 1(b). For this shot the VPF constant was 0.548 km/s/fr. By recording and algebraically manipulating all four outputs, it is possible to extract the phase at each point on the image independently of the neighboring points. This allows us to construct a velocity map averaged over the temporal separation of the two 3 ps probe pulses (263 ps) and over a 1 mm field-of-view with a spatial resolution of ~2-5 μm (Fig. 3(b)).

The raw phase distribution contains a background phase and fixed pattern variations, which have to be characterized during experiments by recording a reference interferogram from the stationary undriven target a few moments prior to the shot. The reference phase is subtracted from the measured phase to produce the shot data with the fixed pattern features removed. Direct summation of the intensity patterns of the four channels also allows a target reflectivity map (non-fringing image) at the 400 nm probe wavelength to be extracted (Figs. 3(c) and (d)). The 2D VISAR employs single mode target illumination and so is more prone than the multimode 1D VISAR to loss of light due to sample roughness when the local angle of the

reflecting surface exceeds the acceptance angle of the VISAR imaging lens ($\pm$ 9.4° for f/3 illumination). The 2D VISAR on Janus was modeled on the original 2D VISAR built at the Omega laser facility. A full description of the diagnostic can be found in ref. 10 with a detailed description of the analysis methodology in ref. 22.

The timing of the 2D VISAR acquisition relative to the time-resolved 1D VISAR record is adjustable shot-to-shot and is measured with optical fiducials to within 20 ps. In order to construct a moving picture of the deformation response of our shocked Si samples we kept the target and laser conditions constant from shot-to-shot while varying the time of the 2D VISAR acquisition. The 1D VISAR provides a record of the compression history within the sample and the 2D VISAR provides a high-resolution spatial map of the Si interface velocity and reflectivity at effective "snapshots" during the compression.

III. Review of Experimental Data

In the following section we report on a number of experiments designed to study the time- and spatial-dependence of high strain-rate deformation in single crystal silicon.

a. Spherical shock through 1 mm thick Si/LiF

The target design for the spherical shock experiments is shown in Fig. 4(a) [and Fig. 1(a)]. As the stress wave reaches the Si/LiF interface the particle velocity as a function of time, $u_p(x, t)$, is recorded with a 1D VISAR along a 2 mm line at the target plane. The raw 1D VISAR data is shown in Fig. 4(b) with the extracted $u_p(t)$ taken at the spatial center of the breakout (x = 0 μm), shown in Fig. 4(c). The VISAR records the arrival of a spatially expanding shock front followed by a velocity plateau arriving at the Si/LiF interface ~88 ns after the initial laser irradiation. The velocity plateau at ~0.25 km/s is equivalent to 4 GPa within the Si sample and is consistent with the elastic limit for Si [111].[7 16] At velocities consistent with the onset of inelastic deformation we observe a drop in the target reflectivity initiating at t = 112 ns and fanning out in space. In successive experiments we kept the drive and target conditions constant while varying the acquisition time for the 2D VISAR. From the 2D VISAR data taken at 114 ns (Fig. 4(d)) it is evident that the elastic and plastic waves have a distinctive three fold symmetrical structure.[23] By considering the reported elastic constants for Si we calculate the elastic wave speed emanating

from the laser ablation surface as a function of angle to produce the expected shape of the elastic wave breakout.[24] As the elastic limit is expected to be overdriven near the laser ablation surface we allow the thickness of the target to vary within this simple model to fit the shape of the measured elastic wave breakout. As shown by the dashed yellow curve in Fig. 4(d) the elastic model gives a good fit to the shape of the elastic wave breakout. We observe plasticity being initiated along the expected slip planes for Si[111] (white line in Fig. 4(d)). The 1D VISAR data in Fig. 4(b) and (c) is sampled along a single vertical line centered on the breakout in the 2D VISAR image in Fig. 4(d) (x = 0 μm).

The 2D VISAR data from similar experiments on single crystal Si [100] and [110] are shown in Fig. 5(a) and (b), respectively. In these experiments there was no circular aperture on the front of the Si samples and as a result the intial compression wave had a slightly irregular shape due to the non-circular laser spot. Consequently, we find the elastic wave fit to our data is not as good as for the Si [111] data. However for the [100] shot in Fig. 5(a) there is a clear four fold symmetry in the center of the shock breakout which is consistent with the expected slip planes (white lines and labels). The structure emerging at the center of the Si [110] sample shows a different symmetry, consistent with the anisotropic deformation response in Si (Fig. 5(b)).

We conclude that the onset of inelastic deformation in Si is due to plastic relaxation along slip planes as opposed to a phase transformation.[25] This is supported by recent measurements which show a transition from a longitudinal to a bulk sound speed at the onset of inelastic deformation; behavior characteristic of plastic deformation and a near complete loss of shear strength.[7] In addition under static compression the lowest pressure phase transformation in Si (diamond structure to β-Sn) has been determined to initiate at ~11.8 GPa whereas we observe inelastic deformation initiating at 4 GPa.[15]

b. Spatially planar shock through 0.3 mm thick Si [111]/LiF

The target design for the planar drive experiments is shown in Fig. 6(a) [and Fig. 1(b)]. The raw 1D VISAR data is shown in Fig. 6(b) along with the extracted Si/LiF particle velocity history, $u_p(t)$, taken at 900 μm with the time axis normalized to the shock breakout time. The velocity profile is consistent with an elastic precursor wave (~0-10ns), traveling at the longitudinal sound speed, separating in time from the slower moving (bulk sound speed) inelastic deformation wave

(initiated at ~10ns).[7] Previous work has shown that there is a polymorphic phase transformation in shock compressed Si [111] initiated at a longitudinal stress of 12.8-14.4 GPa (Si/LiF $u_p \sim 0.8$ km/s).[16] [17] [18] On the 1D VISAR this high-pressure region is marked by a drop in the target reflectivity (Fig. 6(b): $t > \sim 13$ ns and $x > 400$ μm). The $x < 400$ μm region represents the edge of the shock wave with associated lower pressure and higher reflectivity. 2D VISAR data acquired at three times are shown in Figs. 7(a), (b) and (c).

Figures 7(a), (b) and (c) represent 2D VISAR (one channel of raw data) at acquisitions times of 5.5, 12.2 and 18.9 ns, respectively, after arrival of the shock at the window interface. The corresponding peak Si stress states, as shown, are determined from the interface velocity and equation-of-state for Si and LiF.[16] In Fig. 7(a), the 2D VISAR was acquired 5.5 ns after shock breakout and at a longitudinal stress (8.2 GPa) consistent with elastic deformation in Si [111]. The corner of the spatially square compression wave is clearly visible. The elastic shock front has a smooth fringe (velocity) structure. The velocity and reflectivity maps for this shot are shown in Fig. 3. In Fig. 7(b) the 2D VISAR acquisition is at 12.2 ns and a peak longitudinal stress of 10.3 GPa within the Si sample. There are two distinctive regions: a low-pressure elastic region and a central more highly textured high-pressure region. The structure within this region is consistent with the changes in Si/LiF surface texture associated with the emergence of plasticity along overlapping slip planes (Fig. 4(d)). Figure 7(c) shows a 2D VISAR image taken at later times with central Si pressures of ~13.5 GPa. Here the central pressure exceeds the phase transformation pressure and we observe the emergence of a highly speckled texture within the raw data with characteristic feature sizes less than 3-5 μm.

In Fig. 8(a) we show the velocity map extracted from the raw 2D VISAR data shown in Fig. 7(c). Analysis of this highly textured data set is challenging. Poor reflectivity over some regions of the sample made retrieval of the phase information unreliable. Even within the regions of good signal level absolute velocity determination remains ambiguous for the high frequency content. This is due in part to the high precision requirement on the inter-channel spatial registration and also the non-optimal low velocity per fringe constant selected to track the rapidly changing velocity features (see discussion in Sec. IIc). However analysis of regions within the Fig. 8(a) velocity map can provide quantitative estimates of the velocity roughness related to different deformation mechanisms. To that end we select four 150μm^2 regions which represent different states of compression: uncompressed (yellow square), elastic compression (red square), plastic compression (blue square) and phase transformation (black square). To

characterise the velocity structure we calculate the velocity spectral density (power spectrum) as a function of spatial frequency over a frequency interval of 0.02 to 0.5 μm^{-1} (equivalent spatial wavelength interval from 50 μm to 2 μm). This calculation is described in Appendix A and plotted in Fig. 8(b) for the four spatial regions shown in Fig. 8(a). For the plastic and phase transforming regions the spectral power at high frequencies in the analysis should be viewed as a lower bound due to the fringe jump ambiguity discussed above. In the region where the Si is elastically deforming the power spectrum agrees well with the uncompressed Si as would be expected from a 1D uniaxial compression from a planar drive. When inelastic (or plastic) deformation is initiated the clear roughening of the Si/LiF interface (Fig. 7(b)) translates in velocity space to a greater power (over elastically deformed Si) for the spatial frequency range considered. We interpret this structure as being consistent with the emergence of plasticity on slip planes within the Si sample (Sec. IIIa). The structure associated with plasticity, most clearly witnessed in the spherical shock geometry in Fig. 4, becomes more chaotic for planar driven samples as adjacent slip planes overlap and intersect. Shock data from Si/LiF targets have shown that upon initiation of the 12.8-14.4 GPa phase transformation the deformation becomes hydrostatic.[16] In our experiments, with peak stress of 13.5 GPa, we observe a dramatic refinement of the spatial structure of reflectivity emerging at the Si/LiF interface associated with this change in crystal structure (Fig. 7(c)). In the velocity power spectrum (Fig. 8(b)), this effect is seen as enhanced signal versus spatial frequency over the plastically deforming region of the sample. Recent molecular dynamic simulations have found that the onset of a phase transformation in single crystal Ge occurs along shear bands within the material.[25] A similar change in deformation mechanism associated with the phase transformation in Si may be responsible for the refinement of spatial structure we observe in Fig. 7(c) and Fig. 8.

Under shock compression a phase transformation in Si from the ambient semiconductor diamond structure to a high pressure metallic phase has been determined through a measured increase in the sample conductivity by 4-5 orders of magnitude.[32] This would result in an expected *increase* in Si/LiF reflectivity due to the phase transformation. The observed *drop* in Si/LiF reflectivity (Fig. 6(b)) is due, we believe, to the VISAR probe light being scattered outside of the collection angle of the imaging lens due to the sudden roughening of the Si/LiF interface at pressures associated with the phase transformation (see discussion in Sec. II).

Recent work by Turneaure has highlighted the large discrepancy between stress-volume states determined from Si/LiF velocity measurements versus measurements from Si free-surface samples.[16] To address this discrepancy, within the following section we measure the spatial structure emerging at the Si free surface for a comparable compression drive as applied to the Si/LiF samples.

c. Spatially planar shock through 0.3 mm thick Si free-surface sample [111]

The target geometry for the free-surface measurement is shown in Fig. 9. The target is identical to the one used in Sec. IIIb except the LiF window has been removed. We employ the same laser irradiation conditions as described in Sec. IIIb. The raw 1D VISAR data for a typical shot is shown in Fig. 9(b) with the extracted free-surface versus time shown in Fig. 9(c). Unlike the Si/LIF particle velocity data in Fig. 6(b) we note that at peak compression on the Si free-surface sample there is no change in reflectivity. For free-surface targets the stress at the Si-vacuum interface approaches zero. For this reason the VISAR does not reflect off the inelastic deformation surface directly and no resultant drop in target reflectivity is observed. For the free surface sample and after the peak velocity is reached there is a small velocity pull-back followed by a damped velocity oscillation. These features are characteristic of the formation of a spall layer.[26] Spallation occurs as a result of generation of tensile stresses in the interior of a material due to the interaction of forward and backward propagating release waves near the free surface. The spall strength (σ), defined as the tensile stress in a material that results in dynamic fracture, may be approximated[27] from $\sigma \approx 0.5\rho_0 C_b \Delta u_{\mathrm{fs}}$ where ρ_0 is the initial density (2.33 g/cm^3), C_b is the bulk sound velocity at ambient conditions (6.45 km/s),[17] and Δu_{fs} is the change in free surface velocity associated with the velocity pullback at t_0 + 22 ns in Fig. 9(b) (0.1 km/s). This approximation yields a spall strength of ~0.75 GPa, a value significantly lower than the ~8 GPa compressive yield strength.[7] Such high compressive and low tensile strength behavior is characteristic of shock compressed ceramic materials.[29] The 2D VISAR acquisition was recorded at three different times relative to the shock break out as indicated in Fig. 9(c).

Figures 10(a), (b) and (c) represent the non-fringing (photograph) output of the 2D VISAR analysis at acquisitions times of 1.3, 6.3 and 11.3 ns after shock breakout, respectively. The corresponding Si[111] stress states are determined from the free-surface velocity-

longitudinal stress relationship determined from Lagrangian sound speed measurements.[7] At early times (t_0 + 1.3 ns, Fig. 10(a)) localized changes in target reflectivity appear but are blurred as the Si free-surface is outside of the ~5 μm depth of focus of the 2D VISAR imaging system. This blurring effect is more clearly observed in Fig. 11(a) which shows a magnified sub-region from Fig. 10(a) [blue box]. Using a numerical focusing technique a dark feature with a ~2 μm width and a length of ~50 μm comes into focus (Fig. 11(b)).[28] This absence of light in this region represents a local target angle exceeding the acceptance angle of the f/3 imaging optic (± 9.4°). We interpret these dark regions as incipient crack formation or brittle failure at the Si free surface. Over the ~1 mm^2 field of view, the free surface cracks were primarily linear with an average crack separation of ~30-50μm.

The image shown in Fig. 10(b) was taken 6.3 ns after the arrival of the elastic shock at the free-surface. The fracture planes have increased in size with widths up to ~10 μm and lengths up to ~200 μm. Many of the crack features at this time exhibit branching or a three-fold symmetry and have started to connect to adjacent fracture sites. Figure 10(c) shows the image of the silicon free surface 11.3 ns after the arrival of the elastic shock. The fracture planes have largely joined up and formed a fracture network. The line-VISAR for this shot, shown in Fig. 9(b), gives no obvious signature on the development of these fracture features. The average width of the fracture planes at this time is ~20-30 μm which is at or just below the spatial resolution limit of the line-VISAR.

Following the discussion of Grady[29 33], the evolution of brittle failure in the bulk of a shock compressed ceramic material is described by three stages: (1) Above the elastic shock fracture incubation and nucleation is initiated at centers of high shear stress states concentrated on defect sites within the crystal lattice. (2) Continued compression towards peak pressure results in shear fracture and growth within the shock front and (3) at the peak Hugoniot state overlapping shear band networks cause a comminution of the starting material. This description is consistent with our observations in Fig. 10.

A characteristic fracture plane separation, λ, during the initial period of incubation and nucleation (Fig. 10(a)) is derived by Grady[29 33] from energy (driving energy versus fracture surface energy) balance arguments as,

$$\lambda \sim \left(\frac{48\gamma}{\rho\dot{\mu}}\right)^{1/3} \quad , \quad (1)$$

where $\dot{\mu}$ is the shear strain rate, ρ is the material density and γ is the fracture energy. For the $u_{fs}(t)$ profile in Fig. 9(c) we calculate an average longitudinal strain rate,[7] at the time of 2D VISAR acquisition shown in Fig. 10(a), from $\dot{\varepsilon} \sim \frac{du_{fs}}{dt}\frac{1}{2C_L} \sim 2\times10^6$ s^{-1} where the Lagrangian sound speed, C_L, is ~10 km/s.[7] From this we estimate $\dot{\mu} \sim 1.5 \times 10^6 s^{-1}$.[30] For Si[111] and at 8.8 GPa, $\rho \sim$ 2420 kg/m^3 and the fracture energy is $\gamma \sim$1.483 J/m^2.[7 13 31] These values in eqn. 1 give an average spacing between fracture planes of 29 μm, which agrees well with the observations in Fig. 10(a).

Shown in Fig. 12 (a) and (b) are the calculated particle (Si/LiF) and free-surface velocity maps, respectively, for the data shown in Fig. 7(a) and Fig. 10(a) and at times corresponding to the elastic deformation front. Following the prescription described in Appendix A the velocity spectral density or power spectrum was calculated for each velocity field within a representative region of interest (yellow squares in Fig. 12(a) and (b)). Figure 12(c) shows velocity lineouts through Figs. 12(a) and (b) (dashed horizontal lines at 0 μm integrated over a 10μm line width) which show an increase in structure for the Si free-surface sample. Figure 12(d) displays the velocity spectral density for Fig. 12(a) and (b) plotted alongside identical calculations taken from reference (stationary target) images. The Fourier power spectrum from the stationary target has residual power which is due, in part, to phase distortions from air currents within each interferometer arm which affects each pulse differently.[10] Outside of the interferometer all pulses propagate along a common path and so any phase distortions imposed from the environment effect all pulses equally (no impact of velocity determination). As the average u_{fs} value is 1.74x u_p we multiply the Si/LiF trace in Fig. 12(d) by this factor to more readily compare the two datasets (red dashed curve). We find that the Si free-surface target exhibits incipient velocity jetting on spatial scales of ~59 μm (bump in Fourier spectrum) which is not observed for the tamped Si/LiF targets. The bump in the Fourier spectrum for the Si free surface data at 125μm is an additional harmonic of the main jetting spatial feature. The region of interest used to calculate the velocity spectral density was varied in size, orientation and shape (circular versus square) to ensure no finite sampling effects were present.

IV. Discussion

The deformation mechanisms in Si can vary greatly depending on the temperature, strain-rate and nature of compression. Under an applied stress at room temperature Si often deforms through brittle failure due to the characteristically low dislocation flux. At elevated

temperatures or at high strain rates, there is a brittle to ductile transition in Si due to an increased dislocation mobility facilitating plastic flow. Although the temperature rise in our experiments is estimated to be < 75 K at 15 GPa,[32] the confining pressures associated with the uniaxial compression employed here is expected to suppress the onset of brittle fracture while enhancing ductility.[33] [34] Under shock loading Si exhibits high elastic stresses and a near complete loss of shear stress upon the onset of plastic deformation.[17] Our interpretation of the data presented in Sec. III is as follows: above the elastic shock, the onset of inelastic deformation within the bulk and the associated loss of shear strength is consistent with stress relaxation through micro-fracture. However, sample cohesiveness (no open fracture planes) is maintained due to the inertial confinement from the uniaxial compression drive. Experimentally this is evidenced by the absence of cracks at the Si/LiF interface. Upon release at a free surface, however, inertial confinement is no longer satisfied, fracture planes separate and incipient velocity jetting occurs.

Under shock compression, wave speed measurements used to determine the volume collapse associated with the ~12.8-14.4 GPa phase transformation for single crystal Si [111], have produced very different results from free-surface samples and samples with an impedance matched LiF window. Experiments by Turneaure and Gupta[16] on Si/LiF samples report a new phase volume similar to those found in static compression experiments[15] (V/V_0~0.67 at 16 GPa) whereas experiments on free-surface Si samples by Gust and Royce[18] and Goto[17] have reported $V/V_0 \sim 0.85$ at 16 GPa. This large discrepancy was interpreted by Turneaure and Gupta[16] "to originate from differences in the values of [phase transforming shock speed] used in the data analysis. Values reported in the previous work are significantly higher than our measured values." In the free-surface Si experiments we note that the velocity determination was made with an inclined prism technique which relies on the loss of total internal reflection (due to shock impact) within a prism in close proximity to the Si sample.[18] The leading edge of the free-surface release Si is then used to determine the shock velocity and the compressibility associated with the onset of the phase transformation. Our data reveal the presence of stress relaxation and incipient velocity jetting at the Si free surface due to the onset of fracture (Fig. 12); processes not considered within the free-surface measurements which could effect the determination of stress versus volume.

V. Conclusions

The 1D VISAR measures the interface velocity history, *u(x,t)*, of shock compressed Si samples while at different times after the shock breakout the 2D VISAR records the spatially resolved velocity field, *u(x,y)*, over a 263 ps "snapshot" in time. Our data shows the anisotropic response associated with the elastic and plastic deformation in Si. We measure a roughening in particle velocity space consistent with incipient plastic flow along preferred slip planes and a dramatic alteration of the heterogeneous flow with the onset of a structural phase transformation at $\sim$13 GPa. For Si free-surface samples brittle failure is initiated at times less than 1.33 ns after the arrival of the elastic shock. The evolution of crack features observed at the free surface is consistent with a description of an initial fracture nucleation and growth period followed by a more complex onset of network formation. Our data reveals a rich complexity of heterogeneous flow that is not recorded by standard velocimetry techniques and which can have a strong effect on reported stress-density data.

We thank Stephanie Uhlich and Walter Unites for help in the target preparation, Jim Cox for the engineering support in construction of the 2D VISAR and the staff at the Jupiter Laser Facility at LLNL. This work was performed under the auspices of the U.S. Dept. of Energy by Lawrence Livermore National Laboratory under Contract DE-AC52-07NA27344. J.W.'s participation was supported by National Laser User's Facility award DE-NA0000856.

Appendix A

Calculation of velocity spectral density versus spatial frequency (Figs. 8(b) and 12(d))

To characterize the spatial structure within the measured velocity map we first select a region of interest (e.g. square regions in Fig. 8(a)). For a discrete sampling of velocity points V[l,j] (assuming units of m/s) where there are {n,m} pixels in the sample box of physical size $\{L_x, L_y\}$ (units of µm x µm) the {l, j} indices range from 0 to n-1 and 0 to m-1, respectively. We compute the discrete Fourier transform, which yields the mode coefficients:

$C[k_x,k_y]=\sum_{l=0}^{n-1}\sum_{j=0}^{m-1}V[l,j]\mathrm{Exp}[-2\pi i(\frac{lk_x}{n}+\frac{jk_y}{m})]$ where $\{k_x, k_y\}$ are the spectral mode indices ranging from 0 to n-1 and 0 to m-1 respectively. The power spectrum is obtained from the square of the coefficients, and we normalize the result by dividing by {n,m} and applying a factor accounting for the physical size of the analysis box. Therefore, the normalized spectral power density at mode $\{k_x, k_y\}$ is $\left|C[k_x,k_y]\right|^2(L_x\times L_y)/(n\times m)$ in units of $(\text{m/s-}\mu\text{m})^2$. The 1D azimuthal average is an average over the modes contained within set of annular bins spaced to match the pixel size in the Fourier domain. The 1D amplitude spectral density, V_{ASD}, is thus produced by taking the square root of the 1D radially-averaged power spectrum excluding the zero frequency mode (thus producing units of m/s-μm). The spectra are plotted as a function of spectral frequency in units of inverse wavelengths, $f=1/\lambda$. For azimuthally symmetric data sets the velocity RMS can be extracted from V_{ASD} by calculating the expression:

$$V_{rms}=\left[2\pi\int_{f_l}^{f_u}\left(V_{ASD}(f)\right)^2 f\,df\right]^{1/2} \qquad (2)$$

The RMS values are calculated over the frequency interval $[f_L, f_U]$ = [0.02, 0.5] μm^{-1}, which is the wavelength interval from 50 μm to 2 μm (Fig. 8(b)).

Figure 1 [Sec II, Experimental Method Section]

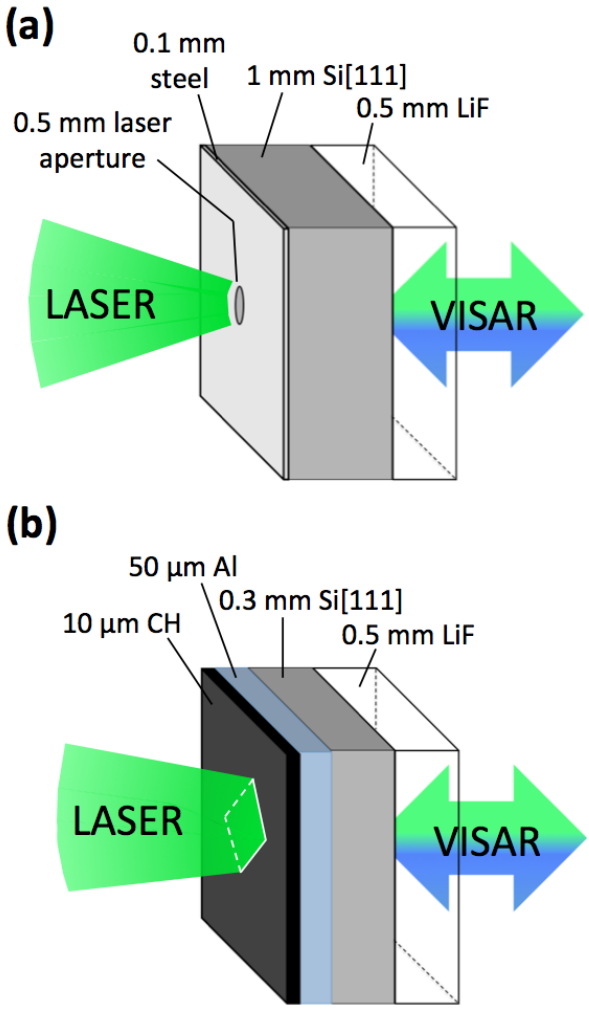

Fig. 1 (a) Target design for spherical shock compression of single crystal Si. The drive laser was focused down to overfill a 0.5 mm aperture within a 100 µm thick stainless steel plate. This ensured a circular pressure drive input to the Si. After shock transit the time dependence and the spatial structure of the Si/LiF velocity was recorded with the 1D and 2D VISAR. (b) Target design for planar shock experiments. In these experiments a 1 mm square planar drive was launched into the target assembly. Experiments were conducted with and without the LiF window. A dual band 532/400 nm anti-reflection coating applied to the LiF free surface ensures no back-reflections of the VISAR probe beam from this interface.

Figure 2 [Sec II, Experimental Method Section]

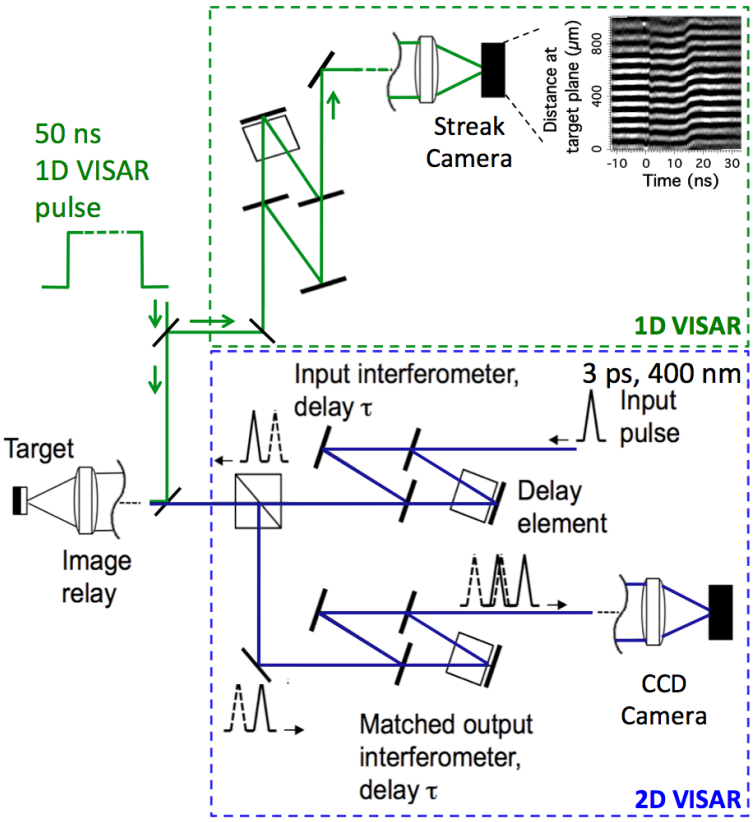

Fig. 2 Layout for diagnostic setup (simplified) for combined 1D and 2D VISAR study of the deformation response of shock-compressed silicon. 2D VISAR layout modified from Ref [10].

Figure 3 [Sec. II, Experimental Method Section]

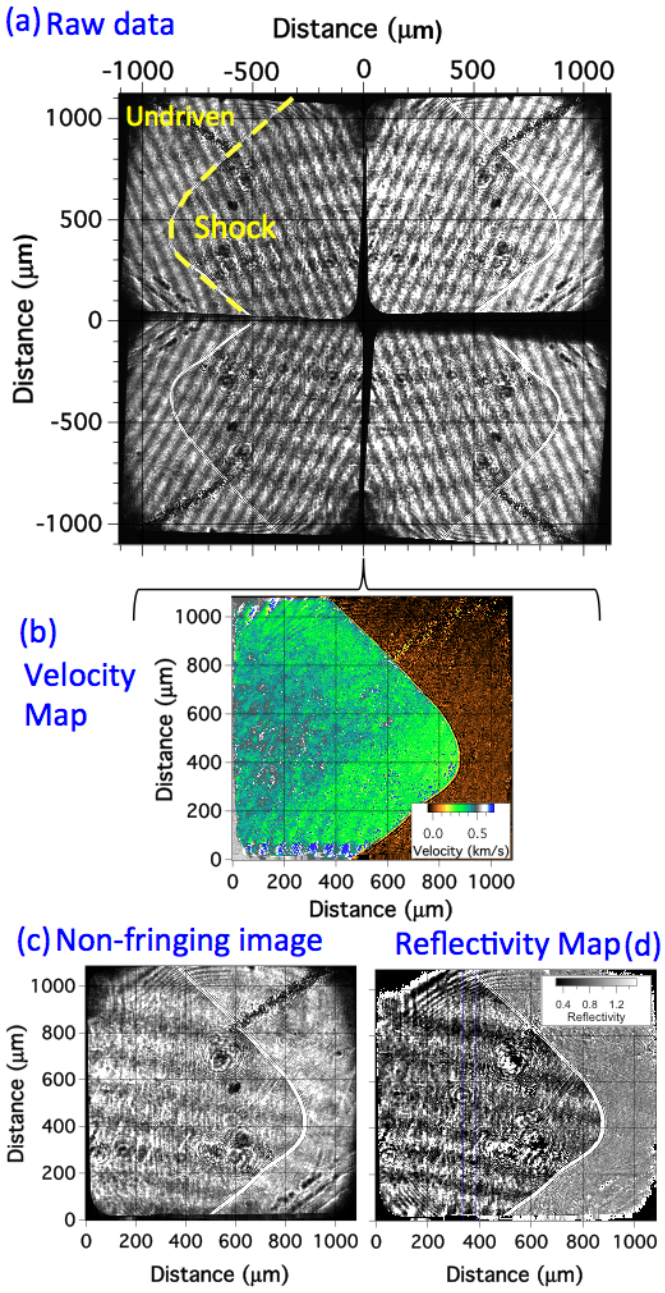

Fig. 3 (a) Four images of the shocked sample are recorded on a 2-inch square CCD chip (shot #070902). Each image shows the corner of the shock wave emerging at the Si/LiF interface from the target described in Fig. 1(b). Two images are from s- and p-polarized light with the other two images being out of phase with their neighbors. (b) The quadrature fringe pattern allows for the velocity map to be determined averaged over the time period set by the delay element within the interferometer plates. (c) Through summation of the four channels a non-fringing image, which is averaged over the reflectivities at the times of the two 3ps pulses, can be generated. The intensity fringes observed running left to right in this image are due to reflections between the Si and LiF interfaces separated by the finite glue layer thickness. Within the shocked region the glue layer thickness changes and the fringe periodicity is modified. (d) Using a pre-shot reference a relative map of reflectivity at 400 nm can be obtained.

Figure 4 [Sec. IIIa, Review of Experimental Data – Spherical Shock through 1mm thick Si[111]/LiF]

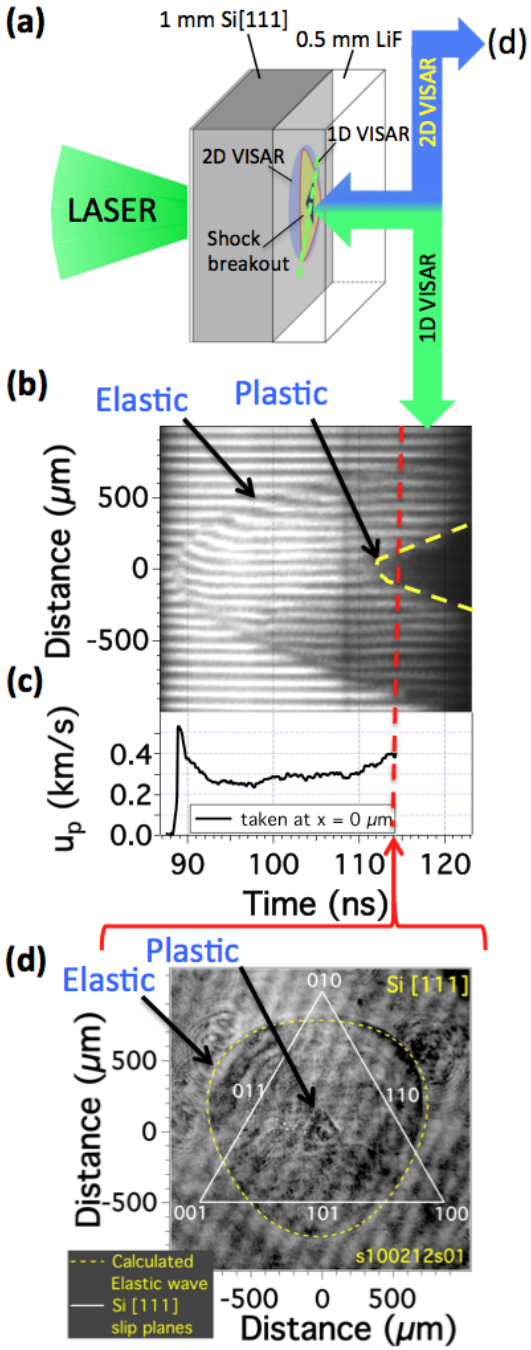

Fig. 4 (a) The target assembly for spherical shock compression of 1 mm thick Si samples (b) The particle velocity history, $u_p(x,t)$, at the Si/LiF interface was measured in one-dimension and over a 2 mm field-of-view with the 1D VISAR. The emergence of a non-planar shock is recorded 88ns after the initial laser irradiation. (c) The extracted Si/LiF $u_p(t)$ at x = 0 μm is consistent with an elastic wave preceeding a slower moving plastic deformation wave.[7] Coinciding with the arrival of the plastic wave at ~112 ns is a sudden loss in reflectivity which fans out in space at later times. (d) The 2D VISAR image taken at 114 ns reveals a three fold symmetry for the elastic and plastic waves. The shape of the elastic wave can be well reproduced by using the elastic constants for Si and calculating the transit time as a function of angle (yellow dashed line). The orientation of the three fold symmetrical plastic wave is consistent with the expected slip planes for Si [111] (white lines with labelled slip planes).

Figure 5 [Sec. IIIa, Review of Experimental Data – Spherical Shock through 1mm thick Si[111]/LiF]

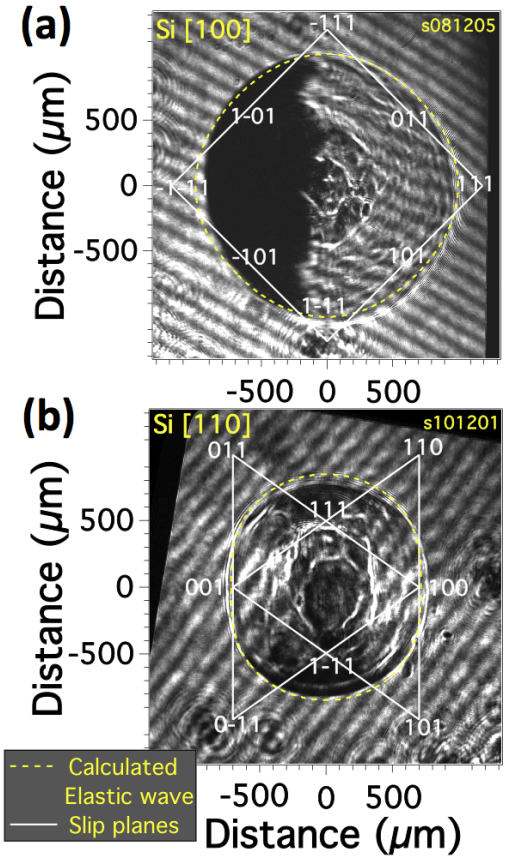

Fig. 5. 2D VISAR data for (a) 1mm-thick single crystal Si [100]/LiF and (b) Si [110]/LiF. In (a) a section of the image is darker as the local angle of the reflecting Si/LiF surface exceeds the numerical aperture of the f/6 imaging system.

Figure 6 [Sec. IIIb, Review of Experimental Data – Spatially planar shock through 0.3mm thick Si[111]/LiF]

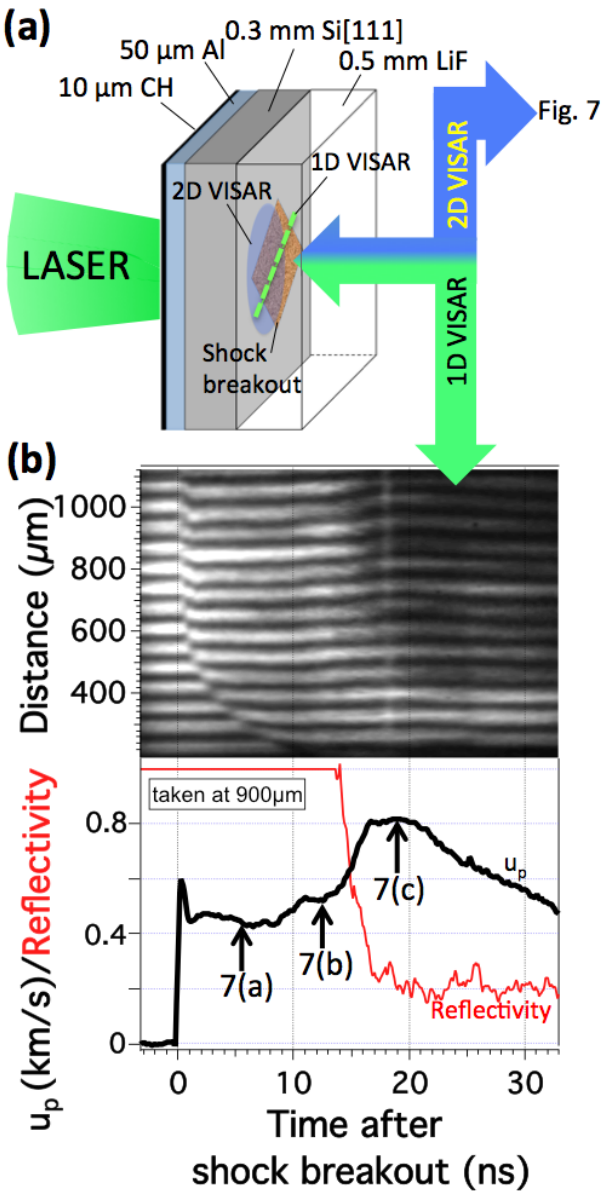

Fig. 6 (a) Target design for planar drive experiments and *in situ* particle velocity measurements. (b) The line VISAR recorded the Si/LiF $u_p(t)$ over a 1mm field-of-view is shown with the extracted Si/LiF particle velocity as a function of time. Three times for the acquisition of the 2D VISAR are indicated and shown in Figs. 7(a), (b) and (c).

Figure 7 [Sec. IIIb, Review of Experimental Data – Spatially planar shock through 0.3mm thick Si[111]/LiF]

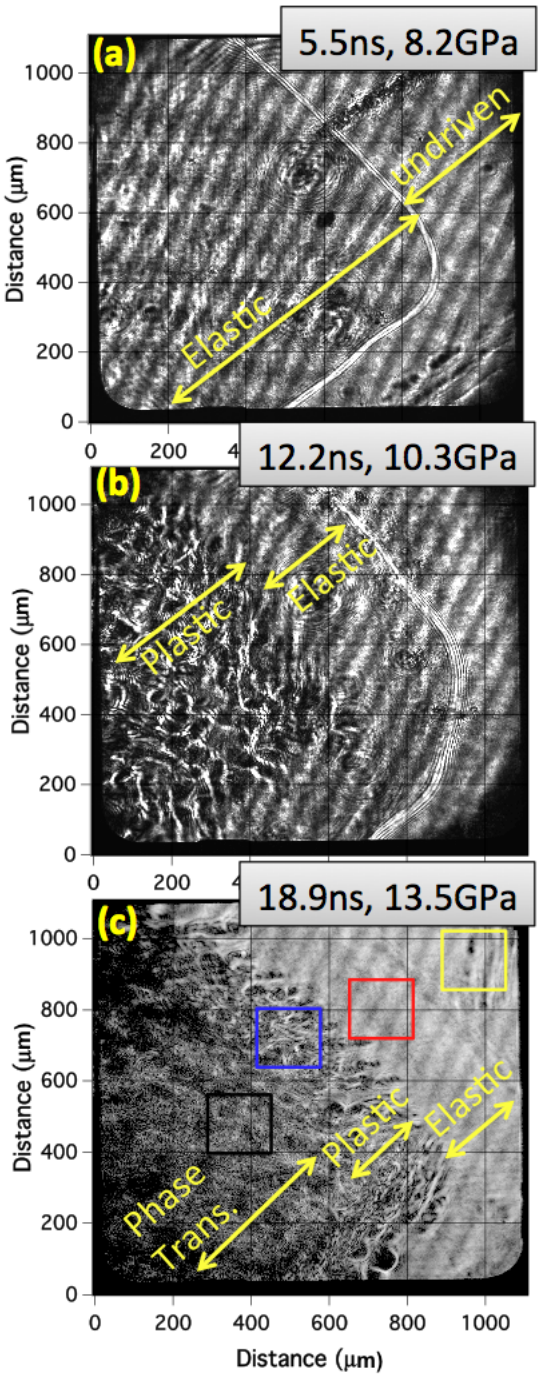

Fig. 7. 2D VISAR images at times indicated in Fig. 6(b). (a) Elastic shock compression exhibits a smooth fringe structure (Shot #070902). The corner of the spatially square shock (from 1mm square laser focal spot) is visible. At later probe time in (b) we observe the smooth low-pressure elastic region skirting the central high pressure plastically deforming portion of the drive (Shot #070903). The structure associated with plasticity is consistent with overlapping slip planes roughening the reflecting Si/LiF surface (Fig. 4(d)). In (c) the peak $u_p(t)$ of 0.8 km/s is equivalent to 13.5 GPa within the Si which results in a structural phase transformation from the ambient diamond structure (Shot #070907).[16] In this high-pressure region we observe a very pronounced change in the surface reflectivity towards a finely speckled pattern with feature size ≤ 3μm. There is also a drop in the reflectivity of the line VISAR data in Fig. 6(b) associated with this high-pressure phase transformation.

Figure 8 [Sec. IIIb, Review of Experimental Data – Spatially planar shock through 0.3mm thick Si[111]/LiF]

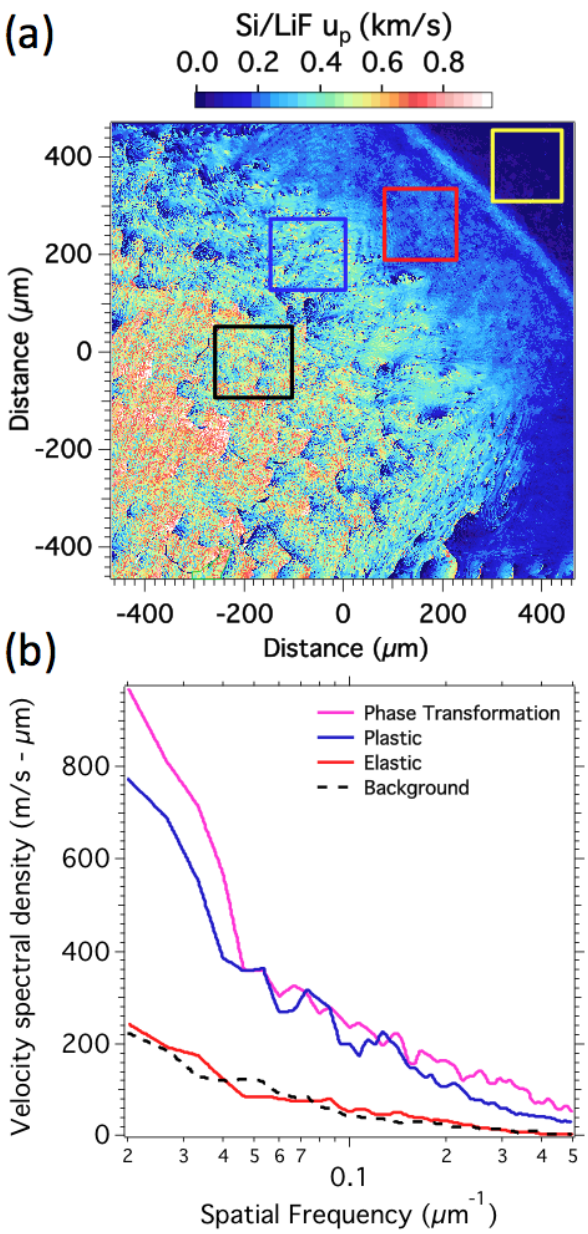

Fig. 8 (a) Velocity Map of image shown in Fig. 7(c) with four squares representing regions of associated with undriven (black), elasticity (red), plasticity (blue) and the phase transformation (pink). The velocity spectral density (see Appendix A) calculated within each of these areas is shown in (b). Roughening of the particle velocity surface is evident for the plastic and phase transformation deformation regions.

Figure 9 [Sec. IIIc, Review of Experimental Data – Spatially planar shock through 0.3mm thick Si[111]]

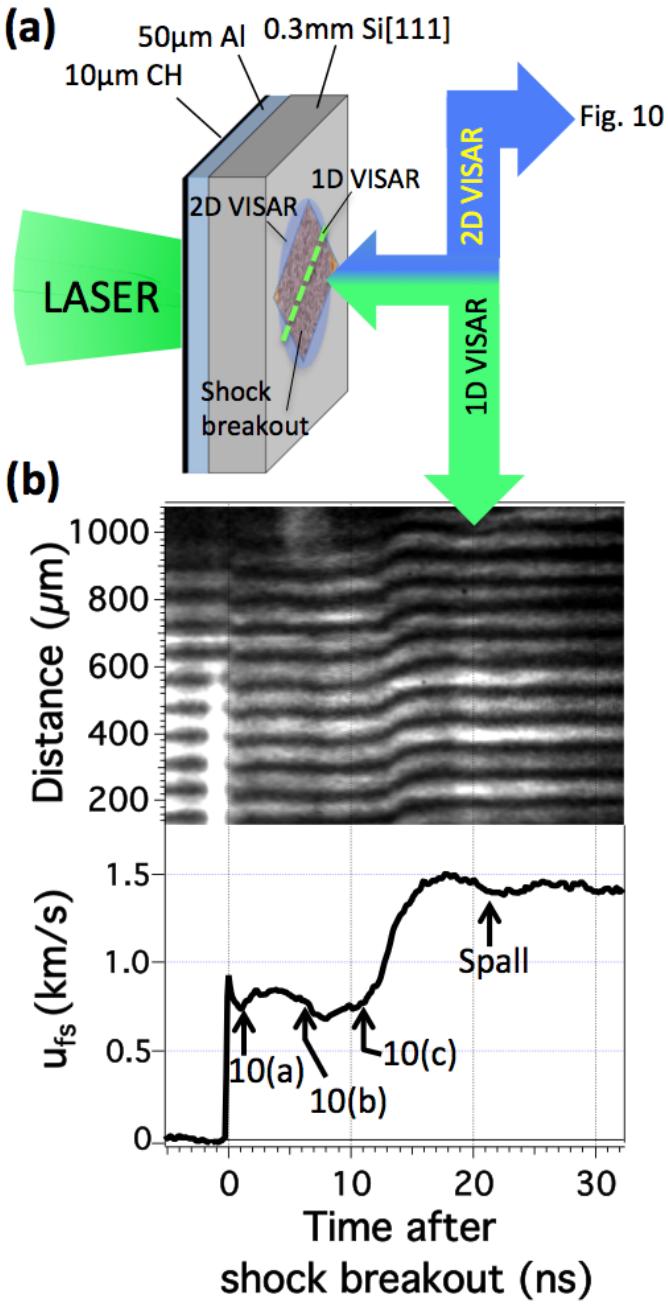

Fig. 9 (a) Target design for free-surface Si [111] VISAR measurements (b) Raw 1D VISAR image. The bright flash at ~0 ns is the optical timing fiducial for the 2D VISAR (c) Extracted free surface velocity history. Three times for the acquisition of the 2D VISAR are indicated and shown in Figs. 10(a), (b) and (c).

Figure 10 [Sec. IIIc, Review of Experimental Data – Spatially planar shock through 0.3mm thick Si[111]]

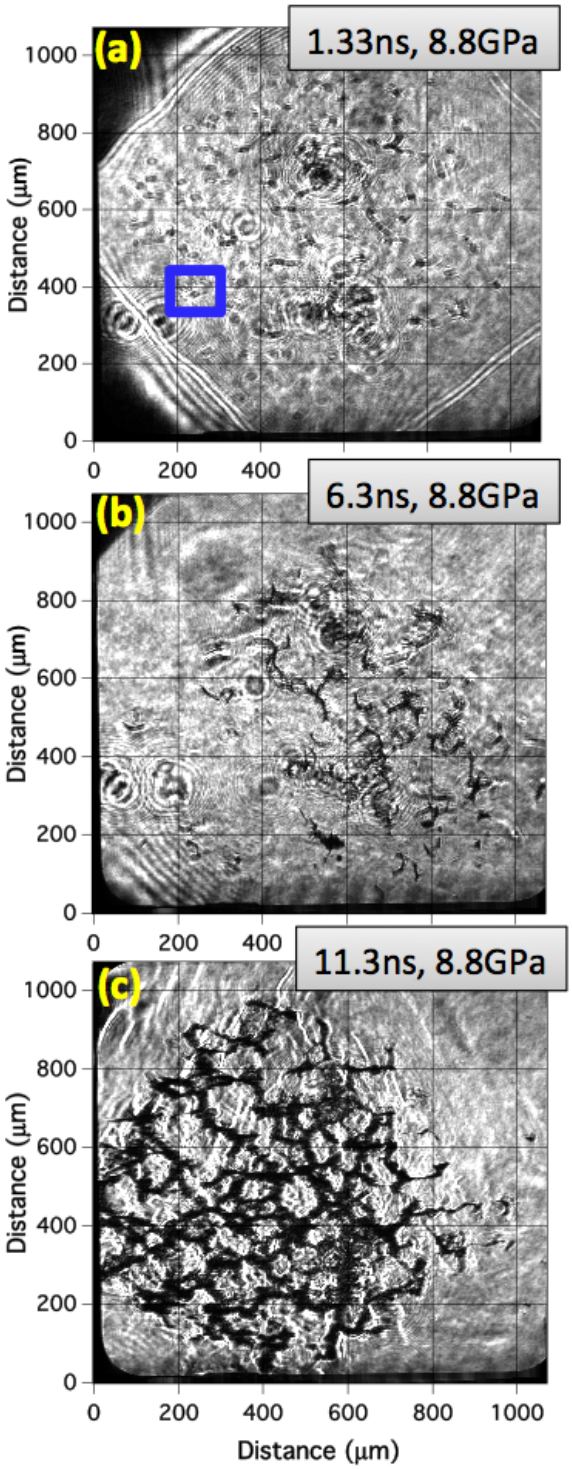

Fig. 10. Non-fringing images (photograph at 400n) for the times indicated in Fig. 9. The blue box in (a) is magnified in Fig. 11 to illustrate the technique of numerical focusing.

Figure 11 [Sec. IIIc, Review of Experimental Data – Spatially planar shock through 0.3mm thick Si[111]]

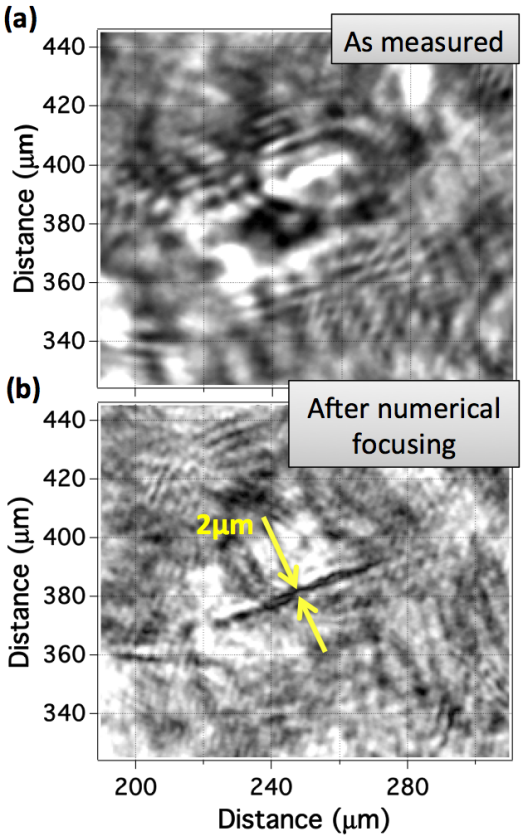

Fig. 11 (a) Shows a subset of Fig. 10(a) [blue box]. Here a feature of the non-fringing image is observed to be out of focus with diffraction lines surrounding the central feature at (x, y) = (240,380) μm. (b) We employ a numerical focusing technique[26] which brings the underlying crack feature into focus with a resolved spatial width of ~2μm.

Figure 12 [Sec. IV, Discussion]

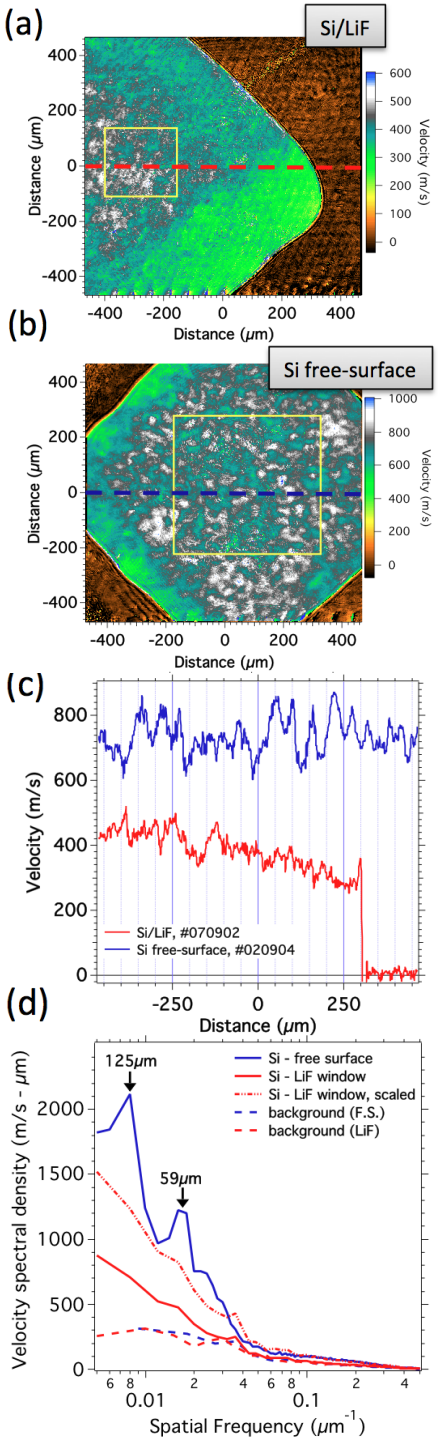

Fig. 12(a) Si/LiF particle velocity map taken within the elastic precursor wave (Fig. 7(a)) (b) Si free-surface velocity map taken within the elastic precursor wave (Fig. 10(a)) (c) Horizontal velocity lineouts through (a) and (b) taken at 0 μm with a 10 μm line width highlight the difference in spatial structure. (d) Comparison of azimuthally averaged Fourier spectrum for free-surface Si (blue curve) and Si/LiF particle velocity (red curve) is consistent with incipient velocity jetting associated with the onset of fracture for the Si free-surface targets.

[1] L. Barker and R. Hollenbach, Rev. Sci. Instrum. **36**, 1617 (1965); L. Barker and R. Hollenbach, J. Appl. Phys. **41**, 4208 (1970); L. Barker and R. Hollenbach, J. Appl. Phys. **43**, 4669 (1972).
[2] W. Hemsing, Rev. Sci. Instrum. **50**, 73 (1979).
[3] Z. Li , R. Ma , G. Chen , J. Liu, J. Yao, Rev. Sci. Instrum. **70**, 3872 (1999).
[4] P.M. Celliers, D.K. Bradley, G.W. Collins, D.G. Hicks, T.R. Boehly, W.J. Armstrong, Rev. Sci. Instrum. **75**, 4916 (2004).
[5] J.-P. Davis, J. Appl. Phys. **99**, 103512 (2006).
[6] Y.M. Gupta, J. M. Winey, P. B. Trivedi, B. M. LaLone, R. F. Smith, J. H. Eggert, and G. W. Collins, J. Appl. Phys. **105**, 036107 (2009).
[7] R.F. Smith, R.W. Minich, R.E. Rudd, J.H. Eggert, C.A. Bolme, S.L. Brygoo, A.M. Jones, G.W. Collins, Phys. Rev. B **86**, 245204 (2012).
[8] J.R. Asay, J. Appl. Phys. **45**, 4441 (1974); J.R. Asay, J. Appl. Phys. **48**, 2832 (1977).
[9] R.F. Smith, J.H. Eggert, M.D. Saculla, A.F. Jankowski, M. Bastea, D.G. Hicks, G. W. Collins, Phys. Rev. Letts. **101**, 065701 (2008).
[10] P.M. Celliers, D.J. Erskine, C.M. Sorce, D.G. Braun, O.L. Landen and G.W. Collins, Rev. Sci. Instr. **81**, 035101 (2010).
[11] M.J. Buehler, H. Tang, A.C.T. van Duin, W.A. Goddard III, Phys. Rev. Letts. **99**, 165502 (2007).
[12] A.M. Lomonosov and P. Hess, Phys. Rev. Letts. **89**, 095501-1 (2002).
[13] R. Pérez and P. Gumbsch, Phys. Rev. Letts. **84**, 5347 (2000).
[14] J.G. Swadener, M.I. Baskes, and M. Nastasi, Phys. Rev. Letts. **89**, 085503-1 (2002).
[15] M.I. McMahon, R.J. Nelmes, N.G. Wright, and D.R. Allan, Phys. Rev. B **50**, 739 (1994).
[16] S.J. Turneaure and Y.M. Gupta, Appl. Phys. Lett. **91**, 201913 (2007).
[17] T. Goto, T. Sato, and Y. Syono, Jpn. J. Appl. Phys. **21**, L369 (1982).
[18] W.H. Gust and E.B. Royce, J. Appl. Phys. **42**, 1897 (1971).
[19] An equivalent plane monitor used to image the laser focal spot before the shot established that there were intensity fluctuations of $\Delta I/I \sim 10$ % over a $\sim$600 μm diameter. Under full amplification, the 600 μm laser spot sits upon a low intensity base which extends to several mm in diameter. To clearly define the spatial input to the Si sample, the laser was focused down to overfill a 500 μm diameter circular aperture (Fig. 1(a)). Any residual spatial structure within the initial pressure drive is expected to be smoothed out as a function of propagation distance within the sample.
[20] R.S. McWilliams, J.H. Eggert, D.G. Hicks, D.K. Bradley, P.M. Celliers, D.K. Spaulding, T.R. Boehly, G.W. Collins, R. Jeanloz, Phys. Rev. B **81**, 014111 (2010).
[21] Spectral Instruments, 800 series CCD camera.
[22] D.J. Erskine, R.F. Smith, C.A. Bolme, P.M. Celliers, G.W. Collins, Rev. Sci. Instr. **83**, 043116 (2012).
[23] For the 2D VISAR data shown in Fig. 4(d) a 75.1173 mm fused silica delay element pair was used in the interferometers which gave a fringe sensitivity of 0.3651 km/s per fringe shift and a temporal separation between the two 3 ps probes pulses of 398 ps.
[24] H.J. McSkimin and P. Andreatch, J. Appl. Phys. **35**, 2161 (1964); H.J. McSkimin and P. Andreatch, J. Appl. Phys. **35**, 3312 (1964).
[25] J.M.D. Lane and A.P. Thompson, CP1195, Shock Compression of Condensed Matter – 2009, edited by M.L. Elert, W.T. Butler, M.D. Furnish, W.W. Anderson, and W.G. Proud, published by the American Institute of Physics (2009).
[26] J. Wang, R.F. Smith, J.H. Eggert, D.G. Braun, T.R. Boehly, J.R. Patterson, P.M. Celliers, R. Jeanloz, G.W. Collins, T.S. Duffy, "Ramp Compression of Iron to 273 GPa", submitted to J. Appl. Phys. (2012).

[27] G. Morard, T. de Rességuier, T. Vinci, A. Benuzzi-Mounaix, E. Lescoute, E. Brambrink, M. Koenig, H. Wei, A. Diziere, F. Occelli, G. Fiquet, and F. Guyot, Phys. Rev. B, **82**, 174102 (2010).

[28] We temporarily Fourier transform the complex image, apply an adjustable cylindrically symmetric parabolic change to the phase, then inverse Fourier transform. The amount of phase change is proportional to the amount of diopters of focal power we are changing the target lens, since the act of Fourier transforming brings an image from the target plane to the pupil plane, and vice versa. See ref: D.J. Erskine, R.F. Smith, C.A. Bolme, S. Ali, P.M. Celliers, G.W. Collins, "New Technologies and Diagnostic Developments", SCCM conference 2013.

[29] D.E. Grady, J. Mech. Phys. Solids **36**, 353, 1988.

[30] For uniaxial strain in a plastically deforming material, the rate of plastic shear strain, $\dot{\mu}$, may be related to the longitudinal strain rate by the following relationship, $\dot{\mu} = \frac{3}{4}\dot{\varepsilon}$. This assumes that the elastic shear strain rate is zero; i.e. that hardening effects due to strain (dislocation density) and strain rate are negligible.

[31] A. Masolin, P.-O. Bouchard, R. Martini, M. Bernacki, J. Mat. Sci **48**, 979 (2013).

[32] S.D. Gilev and A.M. Trubachev, J. Phys.: Condens. Matter **16**, 8139 (2004).

[33] D.E. Grady, Mech. Mat. **29**, 181 (1998).

[34] G.I. Kanel , E.B. Zaretsky, A.M. Rajendran, S.V. Razorenov, A.S. Savinykh, V. Paris, Int. J. Plas. **25**, 649 (2009).